

Army Research Laboratory



**Determination and Use of IR Band Emissivities in a Multiple
Scattering and Thermally Emitting Aerosol Medium**

**By
Robert A. Sutherland**

**Survivability/Lethality Analysis Directorate
Information & Electronic Protection Division**

ARL-TR-2688

July 2002

Approved for public release; distribution unlimited.

20020729 068

NOTICES

Disclaimers

The findings in this report are not to be construed as an official Department of the Army position, unless so designated by other authorized documents.

Citation of manufacturers' or trade names does not constitute an official endorsement or approval of the use thereof.

DESTRUCTION NOTICE—When this document is no longer needed, destroy it by any method that will prevent disclosure of its contents or reconstruction of the document.

Abstract

We report on the application of a fast and efficient method for producing exact solutions of the thermal version of the radiative transfer equation, including effects of multiple scattering from both interior (thermal) sources and exterior (ambient) sources. The method is demonstrated to be accurate to within four significant figures when compared with plane layer solutions published in the literature; this method has the added capability of treating discrete, localized, aerosol clouds of spherical (and cylindrical) symmetry. The method, briefly summarized and applied in earlier papers, is described in detail here where we also demonstrate the utility of the method for calculating emissivity (and reflectivity) functions for finite aerosol clouds of arbitrary optical thickness and albedo. This report is focused on concepts and methods of the PILOT-EX model which forms the theoretical basis for the more practical aerosol effects model PILOT81 designed for use in infrared scene generation and systems analysis. Results here are limited to isothermal clouds, but the study is extended to the more general case in a companion report.

Preface

This is the first part of a two-part study to document the development and verification of the Survivability/Lethality Analysis Directorate PILOT-81 model. The report here (part 1) is focused on major concepts and the follow up (part 2) is focused on verification and other details not covered in part 1. The model as described herein was developed to serve as a natural extension to the existing COMBIC (Combined Obscuration Model for Battlefield Induced Obscurants) model that has served as the U.S. Army standard for several years, which treats only direct transmittance. PILOT-81 was developed as a result of the added requirement to include effects of aerosol thermal emission, or emissivity, into computer-based synthetic scene generation algorithms. The report here is focused on main concepts and fundamental relationships of electromagnetic propagation.

Acknowledgements

The original impetus for this work came, in part, from long-range recommendations set forth by the members of the Survivability/Lethality Analysis Directorate Pilot Project, which originated in 1996. Committee members to be acknowledged are Paul Tannenbaum, Anthony van de Wal, Donald Hemingway, Daniel Hunt, and Lon Anderson. Others who helped with testing early versions of the model(s) include Lee Butler, Jon Anderson, Andre Bevic, James Nealon, and Scarlett Ayres.

Table of Contents

Abstract	i
Preface	ii
Acknowledgements	iii
Executive Summary	vii
1. Introduction	1
2. Hard Targets and Direct Transmission	2
3. Emissive Source Functions and Multiple Scattering	6
4. Methods: Determination of the Source Function	8
5. Results: Source Functions for Isothermal Gaussian Clouds	13
6. Results: Aerosol Emissivity and Reflectivity	18
7. Verification and Comparison with Plane Layers	22
8. Applications: Effects On IR Scene Modeling	24
9. Summary and Discussion	26
References	28
SF 298	30

Figures

1. Sketch demonstrating basic scenario and contributions to total radiance	1
2. Sketch demonstrating concept of source function	9
3. Cumulative effects of multiple scattering on emission and reflection ($t=8.0, w_0=0.99$)	14
4. Relationship between emissive and reflective source functions for isothermal clouds.	15
5. Emissive and reflective source functions for isothermal clouds for various values of albedo and optical thickness	17
6. Summary plots of emissivity and reflective for various values of albedo and optical thickness	19
7. Relationship between exact solutions and one dimensional approximations	21
8. Effect of cloud temperature on IR scene imagery	25

Table

1. Comparisons with plane layers	23
--	----

Executive Summary

This is the first in a series of reports documenting the development and verification of the U.S. Army Research Laboratory (ARL) PILOT-81 aerosol emissive effects model. The original requirement for the model was generated as a part of the Survivability/Lethality Analysis Directorate Pilot Program set up to access both short- and long-term requirements for incorporating realistic atmospheric effects into existing systems analysis studies. The model, as developed, is a natural extension to the existing ARL-COMBIC (Combined Obscuration Model for Battlefield Induced Obscurants) model that has served as the U.S. Army standard for several years. The PILOT-81 study was developed as a result of the added requirement to include effects of aerosol thermal emission and emissivity into existing computer based synthetic scenes used to simulate the modern battlefield. Although the model, *per se*, is focused on the infrared (IR) spectral region it is also applicable in the visible and near IR regions where multiple in-scattering from the external surroundings dominates over internal thermal emission. Although the model is focused on finite three-dimensional Gaussian distributions, it is also valid for the more common plane layer geometry used in conventional existing models. This particular report is focused primarily on theoretical concepts and fundamental relationships of electromagnetic propagation that is the backbone of the more "practical" user version that is described elsewhere. The mathematical method is based on a newly developed iterative approach that, in principle, produces exact analytical solutions for radially symmetric aerosol clouds as well as plane layers.

A major technical barrier encountered in the development of the model was the fact that there are relatively few other methods available for treating the effects of *both* multiple scattering *and* thermal emission in finite clouds. Consequently, relatively few studies exist in the literature with which to compare results. However, our comparisons with the more common plane layer solutions yielded agreement to within five significant figures for the multiple scattering solutions. Besides serving as the baseline for realistic IR scene generation, the results also help verify and define the quantitative limits of various approximations often used throughout the literature and offer a baseline for incorporating effects of multiple scattering and thermal emission that are often not treated in many contemporary obscuration studies. One particularly important case in point is the calculation of the so-named "sky-to-ground" ratio, which is essentially a measure of the aerosol path radiance that, along with the aerosol direct transmittance, forms the basis of many sensor performance models used in U.S. Army wargame simulations such as CASTEFOREM. Further applications and examples of model utilization, verification, and validation are described in follow-on reports.

1. Introduction

The fact that target-background emissivity can have a significant effect on thermal band signatures is well established in current literature, and the theory as applied to natural background surfaces and any other such "hard" targets is well described in standard texts [1]. However, the often equally significant effect of (aerosol) path emissivity as it affects the perceived infrared (IR) signature propagated through a real (obscuring) atmosphere is much less developed, especially in the case where multiple scattering from inhomogeneous "soft" targets, such as localized smoke clouds, can enhance thermal emission while at the same time reducing the (target-background) signal through direct line of sight optical extinction.

A key technical aspect of our work here is the development of a fast and efficient method capable of providing exact analytical solutions for the combined effect of multiple scattering and thermal emission by discrete, localized, aerosol clouds of spherical (and cylindrical) symmetry (fig. 1). For the usual in-scatter case, the underlying theory is well established, being based upon the standard version of the well-known radiative transfer equation, although the mathematical implementation can be difficult even for the relatively simple one-dimensional case for plane layers. However, there are some further complications in dealing with the combined effects of thermal emission and multiple scattering that are not necessarily well established in the obscuring literature that play an important role in practical applications. Only recently have we obtained useful quantitative solutions for the three-dimensional (spherically symmetric) case, including thermal emission, which we report and exploit in this paper. For this particular study we have used an idealized Gaussian aerosol cloud concentration distribution, similar to the U.S. Army COMBIC model [2] and have assumed isotropic scattering, although neither assumption necessarily represents a major restriction on the methods or conclusions.

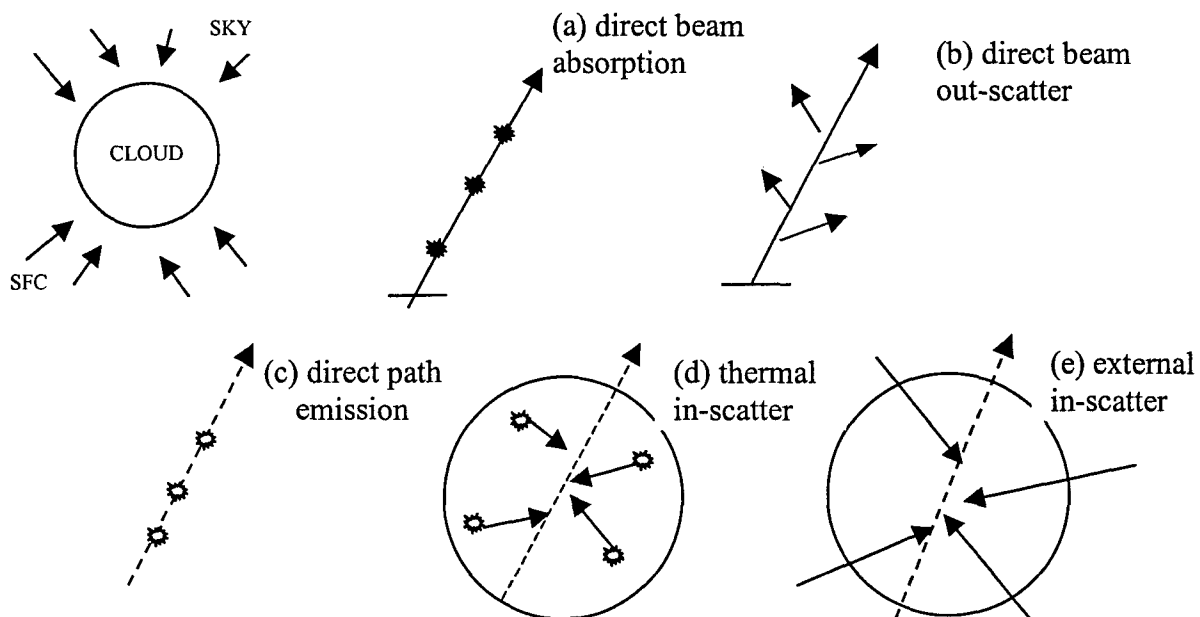


Figure 1. Sketch demonstrating basic scenario and contributions to total radiance.

The basic scenario treated here centers around a finite-sized, self-emitting, (multiple) scattering aerosol cloud of known temperature and albedo assumed to be irradiated from both above and below by plane Lambertian layers to represent incoming external radiation from the sky and surface. The situation is demonstrated in figure 1 where we have also identified the five processes that contribute various components to the total radiation reaching the sensor. That is, referring to the various sketches of figure 1, the direct component is affected by (a) absorption at all points along the main path, and (b) out-scatter at all points along the main path. The diffuse component is affected by (c) direct thermal emission by the aerosol at all points along the main path, (d) thermal in-scatter from all interior points of the cloud, and (e) external in-scatter from the ambient (sky and surface) surroundings. Although not illustrated on the sketches, both the internal thermal emission and in-scatter contributions come from all angles and include multiple scattering and absorption at all interior points along all the multiple paths. In the following sections we examine each contribution in detail using a combination of (1) the "Beer's Law" relationship for the direct transmittance, (2) the underlying Blackbody Laws for direct thermal emission, and (3) appropriately formulated versions of the radiative transfer equation for the in-scattering components.

This report is focused on main concepts and fundamental relationships, some of which have been used and exploited in previous publications [3,4]. Many of the details, including non-isothermal clouds, that are only glossed over here are treated more fully in a companion report [5] which we will henceforth refer to as [5].

In Section 2 we introduce the concept of aerosol emissivity with an analogy based upon the conventional approach for "hard" targets which we expand in Section 3 by introducing the two part radiative source function for "soft" targets (i.e., aerosol clouds) to include both thermal emission and multiple scattering. In Section 4 we describe the mathematical method used for actually computing the radiative source function which we then apply in Section 5 to give some examples for isothermal clouds. In Section 6 we mathematically define the aerosol emissivity and reflectivity and give results based upon the corresponding source functions and fundamental relationships. In Section 7 we give some numerical examples and make comparisons with other models and then, in Section 8, demonstrate the effects on IR scene modeling. Finally, in Section 9 we offer a summary by pointing out some of the advantages and disadvantages of the approach and discuss applications where the results might be used directly in calculating aerosol-induced signal-to-noise ratios for input to IR systems analysis models.

2. Hard Targets and Direct Transmission

Many modeling applications in the past have concentrated on conventional "hard" targets for which the emissivity is defined in terms of the radiance emanating in all forward directions from a classical Lambertian surface as follows:

$$I_{\Delta\lambda}(r_o) = \epsilon_{tgt} B_{\Delta\lambda}^*(T_{tgt}) + r_{tgt} G_{\Delta\lambda}^*(I_{ext})/\pi \quad (1)$$

where $I_{\Delta\lambda}(r_0)$ represents radiance emanating from the background (or "target") surface uniformly in all forward directions. In eq. (1) we have the further condition, $\epsilon_{tgt} + r_{tgt} = 1$, relating the emissivity and reflectivity of the surface in question. The Bandpass function, $B_{\Delta\lambda}^*(T)$, represents the band weighted Planck, or Blackbody, radiance within some specified (sensor) bandpass, $\Delta\lambda$, evaluated at (absolute) temperature, T . The quantity $G_{\Delta\lambda}(I_{ext})$ represents the total incoming hemispherical, or "external," irradiance incident at the target surface and is computed in general as

$$G_{\Delta\lambda}(I_{ext}) = \int_{2\pi} u'_n I_{ext}(\mu', \phi') d\mu' d\phi' \quad (2)$$

where $I_{ext}(\mu', \phi')$ represents incoming radiance from all directions defined by the angular coordinates, (μ', ϕ') , in the forward hemisphere of the target and μ'_n ($\mu = \cos\theta$) is the cosine of the angle between any given incoming ray and the direction of the surface outward normal. In the above equations and throughout we will use the angular coordinates (μ, ϕ) to define any given direction following the usual convention for spherical geometry. For the purposes here, we will also assume the target emissivity, and later, the aerosol mass extinction coefficient and albedo to be constant across the bandpass of interest. This will avoid unnecessary complications at this point; however, there are methods given elsewhere for treating a more detailed wavelength dependence [6].

The physical interpretation of eq. (1) is clear; the first term on the right side represents the magnitude of the inherent thermal emission (radiance) emanating from the material surface, and the second represents reflection of the ambient radiation by the target surface.

The Bandpass function, $B_{\Delta\lambda}^*(T)$, represents the fractional Blackbody radiance within the spectral bandpass, $\Delta\lambda$, of some specified sensor and is computed from the instrument spectral response function, $f_{\Delta\lambda}(\lambda)$, and the Blackbody irradiance, $B(\lambda, T)$ as follows:

$$B_{\Delta\lambda}^*(T) = \left[\frac{\int_0^\infty f_{\Delta\lambda}(\lambda) B(\lambda, T) d\lambda}{\int_0^\infty B(\lambda, T) d\lambda} \right] \frac{\sigma T^4}{\pi} \quad (3)$$

where T is the (absolute) temperature of the radiating surface in question. For the special case of a "flat" spectral response over the full electromagnetic spectrum [i.e., $f_{\Delta\lambda}(\lambda) = 1$], the expression reduces to the simpler Stefan-Boltzman Equation ($B^* = \sigma T^4 / \pi$) as is clear from inspection. In practice eq. (3) and it's inverse are used essentially as a numerical "look-up" table for converting temperature to radiance and vice versa. Methods for efficiently computing the bandpass functions are described in the SPIE (International Society for Optical Engineering) Handbooks and elsewhere[7].

We introduce the concept of optical thickness and direct transmission by applying the Beer's Law of extinction. That is,

$$I_{\text{dir}}(\mathbf{r}_o, \mathbf{r}) = I_{\text{tgt}}(\mathbf{r}_o) e^{-\tau(\mathbf{r}_o, \mathbf{r})} \quad (4)$$

where $I_{\text{dir}}(\mathbf{r}, \mathbf{r}_o)$ is defined as the directly transmitted component and represents that portion of the propagated radiance originally emanating from the target, $I_{\text{tgt}}(\mathbf{r}_o)$, that traverses the intervening medium of optical thickness, $\tau(\mathbf{r}_o, \mathbf{r})$, essentially unimpeded (i.e., being neither scattered nor absorbed). With a little re-arrangement eq. (4) can be taken as a working definition of the optical thickness if the appropriate radiance values are known. Alternatively, if the aerosol mass extinction coefficient is known, the optical thickness can be computed from the path integral of the aerosol concentration, $C(\mathbf{r})$, as follows:

$$\tau(\mathbf{r}_o, \mathbf{r}) = \int_0^{\tau} d\tau' = \alpha \int_0^R C(\mathbf{r}') d\mathbf{r}' \quad (5)$$

where it is understood that the integration proceeds over the straight line path of total length, R , between the location of the target (\mathbf{r}_o) and sensor (\mathbf{r}). In the Gaussian cloud formulation, the concentration path integral of eq. (5), often called the "CL Product" can be calculated analytically, and for the case of spherical symmetry can be written as follows [5]:

$$CL(\mathbf{r}_o, \mathbf{r}; \mu) = \frac{Q_o}{(\sqrt{2\pi}\sigma_o)^3} \int_0^x \exp\left[-\frac{(x' + \mu r)^2 + r^2(1 - \mu^2)}{2\sigma_o^2}\right] dx' \quad (6)$$

where r and r_o are scalar distances referenced from the cloud centroid and μ is the cosine of the angle between the path vector ($\mathbf{r} - \mathbf{r}_o$) and the radial vector \mathbf{r}_o (see ahead fig. 2, Section 4). It is important for later reference to note that the CL Product for this case is a function of the *scalar* distances (r, r_o) and the *relative* angle θ [$\mu = \text{Cos}(\theta)$] as we have indicated in the notation. In eq. (6), the constants Q_o and σ_o are adjustable parameters that control the concentration and distribution half width and are discussed more fully in [5].

In eq. (5) it is of some importance to note that the obscurant mass extinction coefficient, α , includes the effects of both absorption and out-scattering of the direct beam and can be formally separated into the two components as

$$\alpha = \alpha_{\text{abs}} + \alpha_{\text{sca}} \quad (7a)$$

where α_{abs} is defined as the mass absorption coefficient and α_{sca} is defined as the mass scattering coefficient and the two parameters are related through the single-scattering albedo, ω_o , which defines the relative magnitude of the (single) scattering contribution; that is,

$$\omega_o = \frac{\alpha_{\text{sct}}}{\alpha_{\text{abs}} + \alpha_{\text{sct}}} \quad (7b)$$

where it is clear from inspection that an albedo of zero corresponds to total absorption (i.e., no scattering) and an albedo of unity corresponds to total scattering (i.e., no absorption). Both the mass extinction coefficient and single-scattering albedo are assumed to be known constants for the purposes of this paper. Representative values of the optical constants for various bandpasses and aerosol types can be inferred from transmission measurements summarized in the SPIE handbooks [8] or calculated from theory provided that the aerosol bulk properties are known [9].

Although we will later point out significant shortcomings, the Beer's Law expression of eq. (4) is nevertheless important in providing the "direct," or coherent, field representing that part of the propagated radiance reaching the sensor *that actually originated from the target* and as such represents the true usable signal for target sensing. The direct component thus accounts for the first two processes sketched in figure 1. What is not accounted for is the gain of radiation by multiple in-scattering and thermal emission from the ambient surroundings and the cloud interior, *none of which actually originated from the target*. These contributions account for the diffuse, or incoherent, field and can loosely be called the "noise" signal, the calculation of which occupies much of the remainder of this report.

The inclusion of any multiple scattering contributions to the propagated radiance requires a significant modification to the Beer's Law expression that ultimately leads to one form or another of the radiative transfer equation; that is,

$$I(\mathbf{r}_o, \mathbf{r}) = I(\mathbf{r}_o) e^{-\tau(\mathbf{r}_o, \mathbf{r})} + \omega_o \int_0^R \alpha J_{\text{src}}(\mathbf{r}') e^{-\tau(\mathbf{r}_o, \mathbf{r}')} C(\mathbf{r}') d\mathbf{r}' \quad (8a)$$

where the first term represents the familiar Beer's Law contribution and the second formally accounts for all emission and in-scattering processes from either the cloud interior or the ambient surroundings. It may be important in some applications to add a "forward scattering" component to the direct term to separate out any scattered component (not direct) that actually originated from the target. However, this problem is usually treated in a different manner and is not included here.

It is often convenient to recast eq. (8a) entirely in terms of the optical variable, τ , rather than the spatial variable, r , by substituting $[d\tau' = \alpha C(\mathbf{r}') d\mathbf{r}']$ in the second term, in which case we have;

$$I(\mathbf{r}_o, \mathbf{r}) = I(\mathbf{r}_o) e^{-\tau_o} + \omega_o \int_0^{\tau_o} J_{\text{src}}(\tau') e^{-\tau(\mathbf{r}_o, \mathbf{r}')} d\tau' \quad (8b)$$

where we have also substituted $\tau_o [= \tau(\mathbf{r}, \mathbf{r}_o)]$ as the total optical thickness over the target-sensor path distance, R . This transformation turns out to be a particularly important point as it happens that all final expressions will ultimately be cast in terms of the optical thickness, independent of r , *per se*. Often, however, it will be convenient to use the spatial form as a matter of convenience and we will switch back and forth occasionally.

For the case of an infinite plane layer, the solutions to eq. 8 have been known for some time and are well documented in the classic texts [10,11]. Analytical solutions for geometries other than the plane parallel case have usually been limited the extremes of very thin layers where the

single-scattering solutions are known to work well or to very thick layers where the diffusion approximation is known to work well [12]. More recently analytical solutions based upon cylindrical and spherical shapes for atmospheric clouds have been reported [13,14]. Our method here is based, in part, upon an iterative scheme, originally suggested by Van de Hulst [10], that we have adapted to spherical (and cylindrical) geometries using what we call the “source function” approach.

Before continuing it is worth pointing out that there are at least two situations for which the solution to eq. (8) is fairly simple: the first is the trivial case for $J_{src}=0$, which leads to the Beer’s Law solution, and the second is for $J_{src}=Const$, in which case the second term can be integrated immediately to yield

$$I(r_o, r) = I(r_o)e^{-\tau_o} + \omega_o J_{not}(1 - e^{-\tau_o}) \quad (9)$$

where J_{not} is a constant which can either be calculated theoretically, based upon the cloud geometry, or in some cases, estimated empirically from field measurements. It turns out that the form of eq. (9) can be derived in a surprising number of ways, some of which we will discuss later, and is the basis for a number of semi-empirical models which we will ultimately compare with our own exact solutions in later sections.

3. Emissive Source Functions and Multiple Scattering

Stated simply, the immediate task is to calculate the total radiance reaching the sensor, including both those portions emitted by and those portions scattered from the aerosol cloud as well as the direct component from the underlying target. To begin we first re-examine and modify eq.(8) to include effects of thermal emission as well as multiple scattering. To do this in a succinct manner we divide the problem into two parts by expressing the source function as follows:

$$J_{src}(\mathbf{r}) = J_{int}(\mathbf{r}) + J_{ext}(\mathbf{r}) \quad (10)$$

where the first term, J_{int} , accounts for (internal) thermal emission (and the consequent internal multiple scattering thereof) and the second, J_{ext} , accounts for multiple in-scattering of radiation originating from the ambient (external) surroundings. This distinction leads naturally to two expressions replacing eq. (8) which we write here as [5]

optical version :

$$I_{ext}(r_o, r) = I_{dir} + \omega_o \int_0^{\tau_o} J_{ext}(\mathbf{r}') e^{-\tau(r_o, \mathbf{r}')} d\tau' \quad (11a)$$

thermal version :

$$I_{\text{int}}(r_0, r) = J_{\text{dir}} + \omega_0 \int_0^{\tau_0} J_{\text{int}}(r') e^{-\tau(r_0, r')} d\tau' \quad (11b)$$

which we refer to respectively as the “optical” and “thermal” versions of the radiative transfer equation. The optical version has been well studied (at least for plane layers) and accepted by the research community; however, the thermal version although it appears intuitively correct has caused some concern in the past when applied to atmospheric processes. Our version here does require that the system be in local thermodynamic and radiative equilibrium as further discussed elsewhere [15]. In either case, following the usual protocol, we identify the first term in each expression as the direct component and the second as the diffuse component. It is noteworthy that the form of the second expression in both cases are identical; however, as implied by the notation, there is a distinct difference in the direct terms which we write here as

$$\text{optical version :} \quad (12a)$$

$$I_{\text{dir}} = I(r_0) e^{-\tau(r_0, r)}$$

$$\text{thermal version :} \quad (12b)$$

$$J_{\text{dir}} = (1 - \omega_0) \int_0^{\tau_0} B_{\Delta\lambda}^*(T_{\text{cld}}) e^{-\tau(r_0, r')} d\tau'$$

where, in the second expression, T_{cld} is the real (i.e., thermodynamic) temperature of the aerosol cloud, which in general, may be a function of r (or the equivalent τ), and B^* is again the band-weighted Planck, or Blackbody, radiance function applied to the aerosol cloud. The reason for separating out a “direct” term in the thermal version is twofold: the first because of the widespread use as a first approximation, and the second because of the need for consistency in applying the multiple scattering procedures discussed later. The direct term in eq. (12b) represents the cumulative (integral) sum of all “direct” contributions by aerosol thermal emission at all points along the path of integration and as is thus sometimes referred to as the Beer’s Law contribution to thermal emission. Thus, for the trivial case, $J_{\text{int}}=J_{\text{ext}}=0$, both expressions in eq. (11) reduce to the Beer’s Law solutions [16,17].

The above treatment is a very brief description of a complex process that leaves out several important details involving the derivation of the source functions and the processes involved, but which we elucidate upon in succeeding sections. What needs to be pointed here, however, is the fact that once the source functions are known, the calculation of the total radiance is reasonably straightforward, requiring only a simple (numerical) line integration. This latter point represents the practical advantage of the source function approach. The remaining problem, of course, lies in the actual determination of the various components of the source function, which is the subject of the following section.

4. Methods: Determination of the Source Function

The radiative source function can be thought of as a (directionally weighted) measure of the total radiation incident at some given point from all directions over the full 4π steradians of the environmental sphere and can be expressed mathematically at any particular point, \mathbf{r} in the form of the following integral expression:

$$J(\mathbf{r}) = \frac{1}{4\pi} \int \int p(\hat{\mathbf{r}} \cdot \hat{\mathbf{x}}) I(\mathbf{r}, \mathbf{r}_0) d\mu d\phi \quad (13)$$

where the function, $I(\mathbf{r}, \mathbf{r}_0)$, represents the radiance reaching some point, \mathbf{r} , from the direction of the point, \mathbf{r}_0 , along the path, $\mathbf{x} [= \mathbf{x}(\mu, \phi)]$, connecting the two points (fig. 2a).

In figure 2a the incoming arrows represent radiance from all directions and include the effects of thermal emission and multiple scattering by the aerosol cloud, which we assume to be confined within the boundaries of the dashed sphere. The directional weighting factor, $p(\hat{\mathbf{r}} \cdot \hat{\mathbf{x}})$, is known as the scattering "phase" function which describes the angular scattering properties of the underlying aerosol medium and is defined here such that the integration over all angles yields the following relationship:

$$\frac{1}{4\pi} \int \int p(\hat{\mathbf{r}} \cdot \hat{\mathbf{x}}) d\mu d\phi = 1 \quad (14)$$

which, for isotropic scattering, requires that the phase function be set to the constant value of unity, $p(\mathbf{r}, \mathbf{x})=1$, which we will later use in the development. The differential angular coordinates ($d\mu, d\phi$) represent the solid angle [$d\Omega = d\mu d\phi$] centered about the angular coordinates (μ, ϕ) defining an arbitrary propagation path. In theory, the terminal points, \mathbf{r}_0 , extend to infinity, which for our purposes here, can be taken as the practical "edge" of the (Gaussian) cloud represented by the dashed boundary in figure 2.

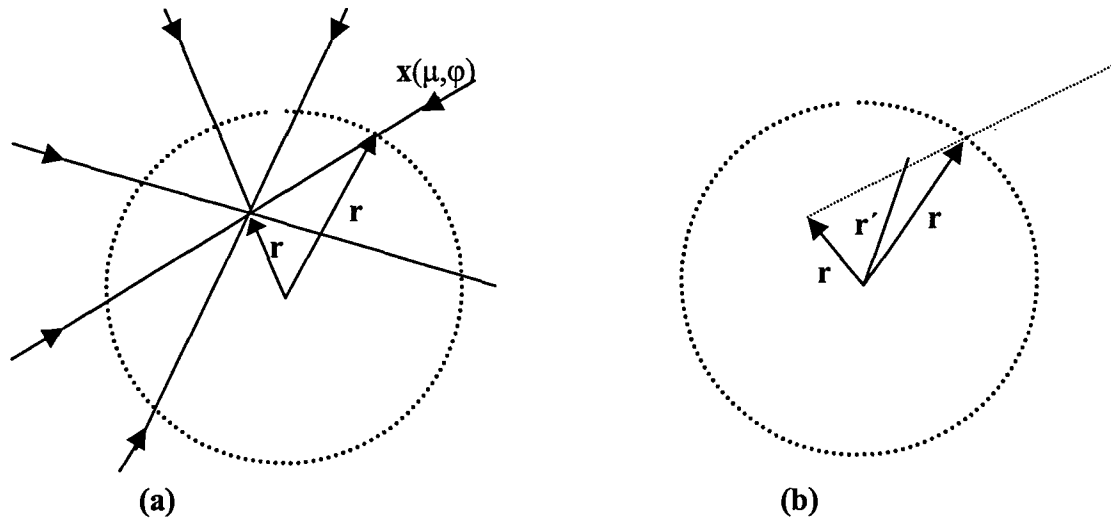


Figure 2. Sketch demonstrating concept of source function.

The major difficulty in evaluating eq. (13) in any direct and simple manner is because the radiance function, $I(\mathbf{r}, \mathbf{r}_0)$, must include all orders of scattering and is itself generally unknown and obtainable only as a solution of the radiative transfer equation which we introduced in Section 2 but rewrite here in a more compact notation as

$$I(\mathbf{r}, \mathbf{r}_0) = I_{\text{dir}} + \omega_0 \int_0^{\tau_0} J(\mathbf{r}') e^{-\tau'(\mathbf{r}, \mathbf{r}')} d\tau' \quad (15)$$

where \mathbf{r}' represents the vector coordinates of any point along the integration path (fig. 2b) and τ_0 $[= \tau(\mathbf{r}, \mathbf{r}_0)]$ is the total path optical thickness. Equation (15) is applicable to either the optical or thermal case as long as we associate the direct term with the appropriate expression based on either eq. (12a) or eq. (12b). It also needs to be pointed out that the expression as written here, including the direct term, applies to *any* direction over the full upper and lower hemispheres and not necessarily to a single "hard" target at a specific location as we had implied in previous sections. When used in this manner our "hard targets" come from the ambient boundary values from all directions over the environmental sphere and are given as input representing the incoming radiances at all points, \mathbf{r}_0 , along the corresponding directions (μ, ϕ) .

The computational method for evaluating eq. (13) for a selected single ray path is demonstrated in the sketch of figure 2b. Note from the sketch that the path of integration begins at the point of interest, \mathbf{r} , and progresses outward along the direction, $\mathbf{x}' [= \mathbf{r}' - \mathbf{r}]$, and terminates at the sensible edge of the cloud (\mathbf{r}_0). At the cloud boundary we assume that the only source of incoming radiation is from the ambient boundary inputs which we will ultimately use to generate the direct term in eq. (15) to compute the external, or reflective, source function contribution.

For a radially symmetric (Gaussian) cloud, it is clear from eq. (6), that the optical thickness along any arbitrary direction is independent of the azimuth and can be expressed in scalar form

as $[\tau(\mathbf{r}, \mathbf{r}') = \tau(r, r'; \mu)]$ where both r and r' in this notation are *scalar* radial distances, referenced from the cloud center and μ is the cosine of the angle between the main computational axis, \mathbf{r} , and the integration path, \mathbf{x}' . With the aid of this result it can furthermore be shown that, for the isotropic case, the radiance function is also independent of azimuth; thus, under these conditions, the integrations over ϕ in eq. (13) can be performed immediately to yield

$$J(r) = \frac{1}{2} \int_{-1}^{+1} I(r, r_o; \mu) d\mu \quad (16a)$$

with

$$I(r, r_o; \mu) = I_o + \omega_o \int_0^{\tau_o} J(r') e^{-\tau'(r, r'; \mu)} d\tau' \quad (16b)$$

where we have set the phase function to unity and have taken advantage of the fact that the source function, under the circumstances cited, is dependent only on the scalar distance, r , independent of the vector orientation of \mathbf{r} . This latter point follows from the fact that the angle associated with μ is referenced relative to \mathbf{r} and not to any fixed axes. It is important to note, at this point, that all distances are scalars and all directional dependence is contained in the single angular variable μ . Equations (16a) and (16b) now take the place of eq. (13) and (15).

Even with the above simplifications, a major difficulty still remains in that the (unknown) source function appears in both expressions, leaving us ultimately with an integral equation to solve. Our approach to a solution is to produce progressively refined (i.e., more accurate) approximations using an iterative scheme based on the following pair of equations relating any iterate of J_{n+1} to the previous iterate of I_n as

$$J_{n+1}(r) = \frac{1}{2} \int_{-1}^{+1} I_n(r, r_o; \mu) d\mu, \quad n = 1, 2, 3, 4, 5 \quad (17a)$$

with

$$I_n(r, r_o; \mu) = I_o + \omega_o \int_0^{\tau_o} J_n(r') e^{-\tau'(r, r'; \mu)} d\tau' \quad \dots n = 1, 2, 3, 4 \quad (17b)$$

where, with $[\tau_o = \tau(r, r_o; \mu)]$, we can use either the spatial (r) or optical (τ) representations in a consistent scheme. The first order solutions to initiate the procedure are treated as special cases, the forms based upon the boundary conditions for the reflective cases and from physical arguments for the emissive case. That is, for the emissive case we have for the first iterate, the simple direct term

$$\begin{aligned} I_o &= 0 \\ J_1(r) &= (1 - \omega_o) B_{\Delta\lambda}^*(T_{\text{clid}}), \text{ emissive case} \end{aligned} \quad (18)$$

where the second expression follows directly from eq. (12b). For the reflective cases we have, for the first iterate, the "single scattering" term which follows from elementary considerations:

$$\begin{aligned}
I_o(r, \mu) &= I_\infty(r_o; \mu) e^{-\tau(r, r_o; \mu)} \\
J_1(r) &= \frac{1}{2} \int_{-1}^{+1} I_\infty(r_o; \mu) e^{-\tau(r, r_o; \mu)} d\mu \quad \text{reflective case}
\end{aligned} \tag{19}$$

where the values of $I(r_o, \mu)$ come from the boundary conditions representing the incoming sky and surface radiances and are assumed known constants for the examples to follow.

With the first order solutions so determined, we begin the iteration process by calculating the first order radiance, I_1 . This is done by substituting the first order source function, J_1 , into eq. (17b); thus,

$$I_1(r, r_o; \mu) = I_o + \omega_o \int_0^{\tau_\infty} J_1(r') e^{-\tau'(r', r; \mu)} d\tau' \tag{20}$$

from which the solution for the second order source function is found by substituting this result into eq. (17a) to obtain

$$\begin{aligned}
J_2(r) &= \frac{1}{2} \int_{-1}^{+1} I_1(r, r_o; \mu) d\mu \\
&= \frac{1}{2} \int_{-1}^{+1} I_o d\mu + \frac{1}{2} \left\{ \int_{-1}^{+1} \left[\int_0^{\tau_\infty} J_1(r') e^{-\tau'(r', r; \mu)} d\tau' \right] d\mu \right\} \\
&= J_1(r) + \Delta J_1(r)
\end{aligned} \tag{21}$$

where, for clarity, we have included the necessary intermediate steps. In eq. (21) the substitution for $J_1(r)$ follows directly from the definition given by eq. (17b). The form of ΔJ_1 is clear from inspection; that is, from the second term in the middle expression we have

$$\Delta J_1(r) = \frac{1}{2} \left\{ \int_{-1}^{+1} \left[\int_0^{\tau_\infty} J_1(r') e^{-\tau'(r', r; \mu)} d\tau' \right] d\mu \right\} \tag{22}$$

which can be applied to either the thermal or reflective cases so long as we make the appropriate distinction for $J_1(r)$. With $J_2(r)$ so determined from eq. (21), the second order radiance becomes

$$\begin{aligned}
I_2(r, r_o; \mu) &= I_o + \omega_o \int_0^{\tau_\infty} J_2(r') e^{-\tau'(r', r; \mu)} d\tau' \\
&= I_o + \omega_o \int_0^{\tau_\infty} J_1(r') e^{-\tau'(r', r; \mu)} d\tau' + \omega_o \int_0^{\tau_\infty} \Delta J_1(r') e^{-\tau'(r', r; \mu)} d\tau' \\
&= I_1 + \omega_o \int_0^{\tau_\infty} \Delta J_1(r') e^{-\tau'(r', r; \mu)} d\tau'
\end{aligned} \tag{23}$$

where we have again included the intermediate steps. Continuing in a straightforward manner we have, for third order, and including the intermediate steps

$$\begin{aligned}
 J_3(r) &= \frac{1}{2} \int_{-1}^{+1} I_2(r, r_0; \mu) d\mu \\
 &= \frac{1}{2} \int_{-1}^{+1} I_1 d\mu + \frac{1}{2} \int_{-1}^{+1} \left[\int_0^{\tau_\infty} \Delta J_1(r') e^{-\tau'(r', r; \mu)} d\tau' \right] d\mu \\
 &= J_2(r) + \Delta J_2(r)
 \end{aligned} \tag{24}$$

and again, making the appropriate substitutions, we have for the third order radiance

$$\begin{aligned}
 I_3(r, r_0; \mu) &= I_0 + \omega_0 \int_0^{\tau_\infty} J_3(r') e^{-\tau'(r', r; \mu)} d\tau' \\
 &= I_0 + \omega_0 \int_0^{\tau_\infty} J_2(r') e^{-\tau'(r', r; \mu)} d\tau' + \omega_0 \int_0^{\tau_\infty} \Delta J_2(r') e^{-\tau'(r', r; \mu)} d\tau' \\
 &= I_2 + \omega_0 \int_0^{\tau_\infty} \Delta J_2(r') e^{-\tau'(r', r; \mu)} d\tau'
 \end{aligned} \tag{25}$$

from which the trend is now clear. Indeed, continuing on for as many steps as necessary, we arrive at the following generalization:

$$I_{n+1}(r, r_0; \mu) = I_n(r, r_0; \mu) + \omega_0 \int_0^{\tau_\infty} \Delta J_n(r') e^{-\tau'(r', r; \mu)} d\tau' \tag{26a}$$

and

$$J_{n+1}(r) = J_n(r) + \frac{1}{2} \int_{-1}^{+1} \left[\int_0^{\tau_\infty} \Delta J_n(r') e^{-\tau(r, r'; \mu)} d\tau' \right] d\mu \tag{26b}$$

where in all steps we have

$$\Delta J_n(r) = J_n(r) - J_{n-1}(r) \tag{26c}$$

which is the final solution appropriate for any order and is the form actually used in our algorithms for generating the source functions for both spherical and plane layer symmetry.

In applying the above equations an approach was used for repeatedly testing successive orders until a convergence criteria was met. For all cases to follow the convergence criteria was based on the value of the line integrated quantity,

$$X = \int_0^{\tau_o} J(r) e^{-\tau} d\tau \quad (27)$$

which was performed at the end of each iteration, and in which case the calculations were terminated if the change did not exceed a preset threshold value of 10^{-6} . In all cases treated this led to a well-behaved solution for all orders that resulted in a smooth monotonic approach to convergence as will later be demonstrated. As may be expected, it was generally found that the number of orders required for convergence increased with increasing albedo and cloud optical thickness. The most extreme case ($\omega_o=1$, $\tau_o=8$) required on the order of 500 iterations. For all examples to follow, the spatial resolution was determined by incrementing in equal units of (normalized) optical thickness providing 100 points over the full range (i.e., $\Delta\tau=0.01$). Angular resolution provided for 21 equal solid angle increments over the full 4π angular range of integration.

5. Results: Source Functions for Isothermal Gaussian Clouds

An example of how the iterative method works through the various scattering orders is shown in the plots of figure 3 where we include the various intermediate solutions leading up to the final convergent solution (represented by the extreme upper curve in both cases). Plots on the left represent the reflective case and those on the right represent the emissive case. In both cases the abscissa represents the cloud edge-to-edge optical thickness, τ/τ_o , normalized to unity and numerically equivalent to the path integrated concentration or CL Product discussed previously in connection with eq. (5) and (6). In all cases the ordinate is the (normalized) source function defined as

$$\hat{J}_{\text{int}}(\tau_o, \omega_o; r) = \frac{J_{\text{dir}}(\tau_o, \omega_o; r)}{B_{\Delta\lambda}^*(T_{\text{cld}})} + \omega_o \frac{J_{\text{int}}(\tau_o, \omega_o; r)}{B_{\Delta\lambda}^*(T_{\text{cld}})} \quad (28a)$$

and

$$\hat{J}_{\text{ext}}(\tau_o, \omega_o; r) = \omega_o \frac{J_{\text{ext}}(\tau_o, \omega_o; r)}{B_{\Delta\lambda}^*(T_{\text{ext}})} \quad (28b)$$

where T_{cld} and T_{ext} represent, respectively, the cloud (real) temperature and the ambient (radiative) temperature where both are assumed constant. In eq. (28) we have also modified the notation to make it explicit that the form of the source function, given that we have a finite Gaussian cloud, depends upon both the aerosol albedo, ω_o , and the cloud total edge-to-edge optical thickness, τ_o , as will be apparent in later paragraphs.

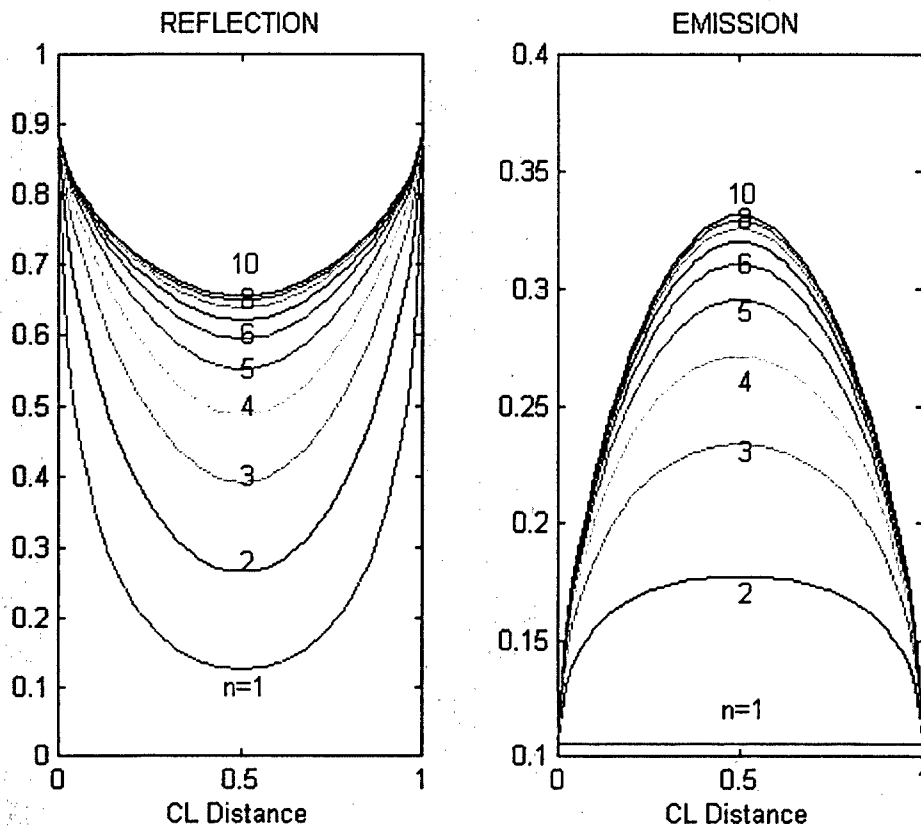


Figure 3. Cumulative effects of multiple scattering on emission and reflection ($t=8.0, \omega_0=0.99$).

For the particular example shown in figure 3, we have used a value of $\tau_0=4.0$ for the total cloud optical thickness and a value of $\omega_0=0.905$ for the albedo, values which happen to be convenient for demonstrating the effects of multiple scattering. The various curves in either case represent order of scattering beginning with the first order solution ($n=1$) at the extreme bottom and proceeding through 10 successive orders which, in this example, is the number of iterations required for convergence based upon the criteria of eq. (27).

Clearly all plots in figure 3 are symmetrical about the cloud center and tend to converge at the edges to a constant value near either $\omega_0 (=0.905)$ for the reflective case or $1-\omega_0 (=0.895)$ for the emissive case. A significant feature of the plots is that, for all orders, the reflective curves are concave up and the emissive curves are concave down (with the exception of the first order emissive solution, $n=1$, which is perfectly flat). Overall, in both cases all curves monotonically increase point by point with increasing scattering order and are generally well behaved and qualitatively predictable.

For the reflective case the first order solution reaches a broad minimum at a value of approximately $J_{\text{ext}}=0.12$ near the cloud center. The overall behavior of the higher order solutions may be explained from elementary considerations based on the fact that light penetration would be most difficult deep in the cloud center, especially for an optical thickness of 4.0. As the scattering order increases, the curves become broader as more light penetrates the interior, and the center values increase, eventually reaching a maximum of about $J_{\text{ext}}=0.70$ for the convergent solution with little or no change at the edges. For the emissive case the first order curve is

perfectly flat and represented by a constant at a value equal to $(1 - \omega_0)$, as it must be according to eq. (28). The other curves behave much like the reflective case: the higher order solutions build up in the middle, approaching, in this case, a maximum value between 0.30 and 0.35 for the convergent solution and little or no change at the edges.

A significant feature of the two plots when examined together is that the final convergent solutions for the two cases seem to be inverted images of each other; that is, one is concave upward (reflective) and the other is the concave downward complement (emissive). This relationship may be difficult to discern directly from figure 3 because of the different scales but is more clearly shown in the examples of figure 4 to follow.

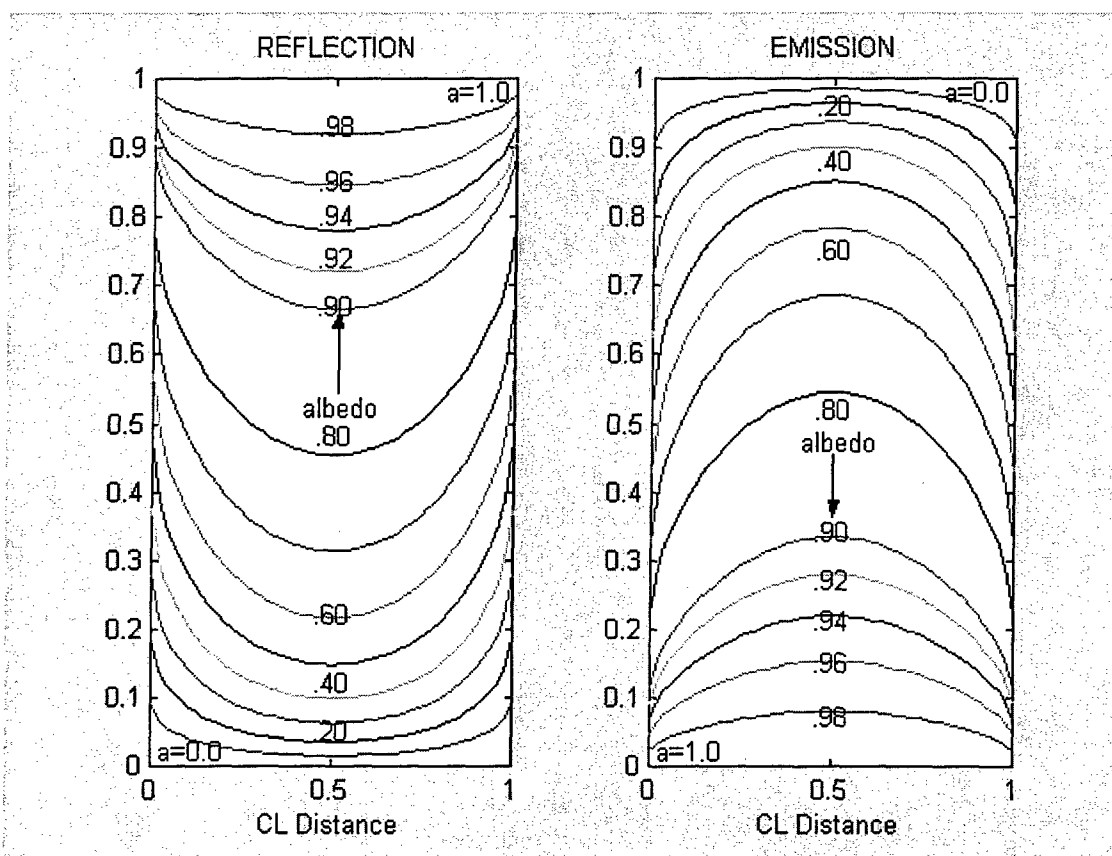


Figure 4. Relationship between emissive and reflective source functions for isothermal clouds.

In figure 4 we show the final convergent solutions only for a wide variety of albedos and again use a cloud optical thickness of 4.0 as an example as show results for both the reflective (left) and emissive (right) cases. The various curves in each subfigure represent the albedo ranging in value from $\omega_0=0$ to 1 in increments of $\Delta\omega=0.10$ with the exception between 0.90 and 1.0, where we use an increment $\Delta\omega=0.02$. The apparent asymmetry between the two cases is immediately clear from the inspection: the reflective curves tend to be concave upward and the emissive curves tend to be concave downward in what looks to be complimentary counterparts. Note also the reversal in the ordering of the curves wherein the reflective curves increase in overall magnitude with increasing albedo (upward) and the emissive curves decrease in overall magnitude with increasing albedo (downward), suggesting a simple complimentary relationship which we will later verify. In this particular example the broadening, or "flattening out," of the

curves as the albedo decreases for the reflective case or increases for the emissive case is also readily apparent. Although not shown explicitly on the plots, but clear from the trends, the curves ultimately collapse to straight lines on either zero axis (reflective case) or the unity axis (emissive case) as the albedo approaches either zero or one, respectively. It also happens that the curves for the other extreme also collapse to either unity (reflective case) or zero (emissive case) as the albedo approaches either one or zero, a trend that is most evident from the curves between 0.90 and 1.0. This “collapse” in different directions either to unity or zero at both limits of the albedo occurs for all examples to follow, but is most apparent at the higher values of optical thicknesses and has some interesting ramifications as will be pointed out in subsequent sections. As noted before in the discussion of figure 3, it is apparent, in all cases, that the magnitudes at the cloud edges approach a value near ω_0 for the reflective case and $(1-\omega_0)$ for the emissive case.

Further study of the underlying equations and numerical results eventually confirmed that the separate solutions for the emissive and reflective cases are, indeed, exact compliments of each other, and expressly related as follows:

$$\hat{J}_{\text{ext}}(\tau_0, \omega_0; \tau) + \hat{J}_{\text{int}}(\tau_0, \omega_0; \tau) = 1 \quad (29)$$

which is a very important relationship that was found to be valid for the full range optical thickness and albedo investigated using the full multiple scattering procedure from Section 3. This result clearly has some immediate practical ramifications; the most obvious being that we need only to perform the (lengthy) multiple scattering calculations once, either reflection or emission, and then find the other through eq. (29). It later turns out that both cases are related to the generalized “embedded sources” approach suggested by van de Hulst for the case of plane layers [10]. One note of caution, however, is that all results here apply *for the isothermal case only*. Modifications for treating the effects of temperature stratification are investigated in [5].

We summarize the findings for the isothermal case in figure 5 with plots of the calculated reflective and emissive source functions covering a wide range of albedo and full-cloud optical thickness. As usual we show the six reflective cases on the left and the corresponding six emissive cases on the right. In both cases, the labeling of the curves for various albedo follows the same legend as in figure 4 wherein the magnitude of the reflective curves all increase with increasing albedo and the magnitude of the emissive curves all decrease with increasing albedo as we have indicated on the uppermost subfigures. In all cases the emissive-reflective pairs are related according to eq. (29), although we used the full iterative solution to generate the results here as a check of the procedure. The six subplots in each case cover the range of cloud optical thickness from $\tau_0=0.250$ to $\tau_0=8.0$ and, as before, 11 values of albedo ranging from $\omega_0=0$ to 1 in equal increments (note that the extremes for, $\omega_0=0$ and 1, are flat lines coincident with the upper and lower axes and not discernable on the plots). It is clearly evident that the curves are all well behaved and predictable in a qualitative fashion. A most striking feature evident from inspection of the set as a whole is that the curves are almost completely flat at the lower values of optical thickness (upper plots) with a near constant value of either ω_0 (reflective) or $1-\omega_0$ (emissive). It is also evident in all cases that as the cloud optical thickness increases, the values in the cloud center tend to either decrease (reflective) or increase (emissive) while also tending to maintain constant values at the edge giving rise to the increased curvature. As pointed out in the discussion of figure 4, all curves “collapse” to either unity or zero as the albedo approaches

either extreme of $\omega_o=1$ (complete scattering) or $\omega_o=0$ (complete absorption) for all values of optical thickness.

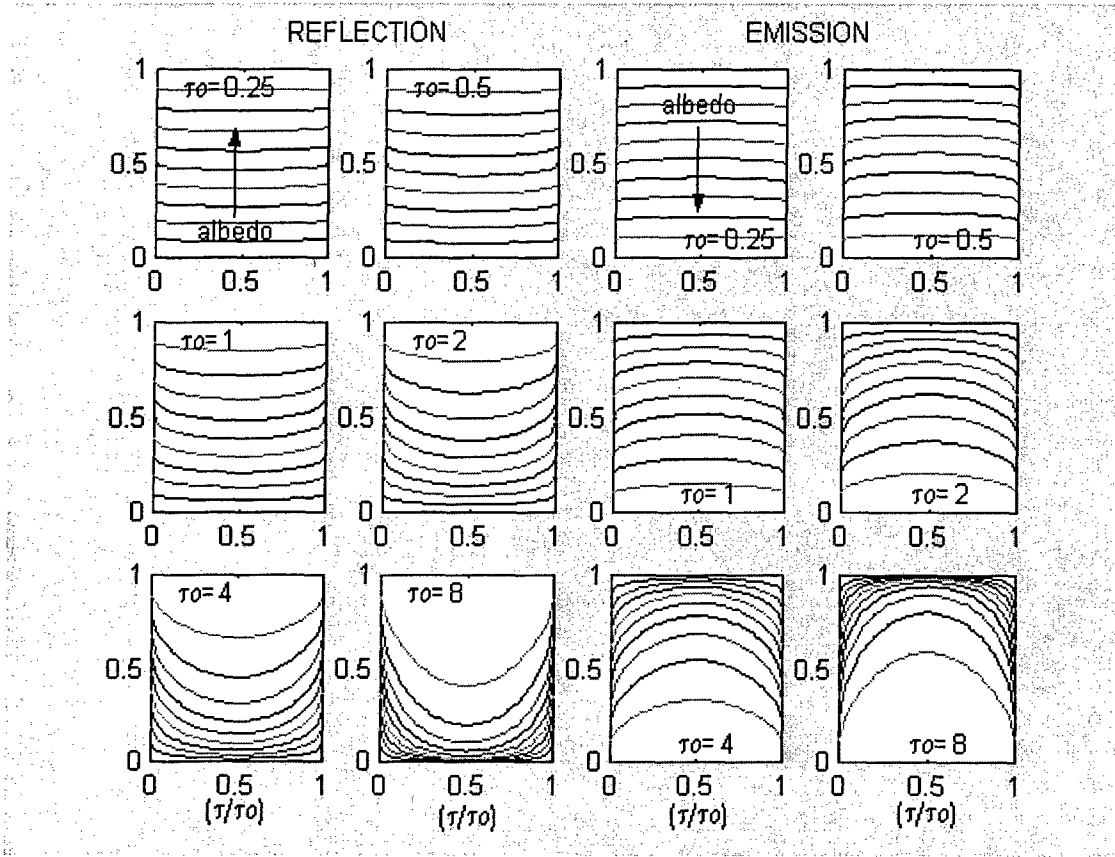


Figure 5. Emissive and reflective source functions for isothermal clouds for various values of albedo and optical thickness.

We summarize this section and demonstrate the utility of the source functions by rewriting the radiative transfer equation in an “engineering” form more suitable for applications, given that the source functions are known, as

$$I(\mathbf{r}_o, \mathbf{r}) = I(\mathbf{r}_o) e^{-\tau(\mathbf{r}_o, \mathbf{r})} + B_{\Delta\lambda}^*(T_{\text{ext}}) \int_0^{\tau} \hat{J}_{\text{ext}}(\tau_o, \omega_o; \tau') e^{-\tau'(\mathbf{r}_o, \mathbf{r})} d\tau' + B_{\Delta\lambda}^*(T_{\text{cld}}) \int_0^{\tau} \hat{J}_{\text{int}}(\tau_o, \omega_o; \tau') e^{-\tau'(\mathbf{r}_o, \mathbf{r})} d\tau' \quad (30)$$

where the temperatures T_{cld} and T_{ext} are assumed known. Equation (30) is valid for all propagation paths passing along any angle and penetrating any portion of the cloud.

6. Results: Aerosol Emissivity and Reflectivity

Following the strict physics protocol, we define the aerosol cloud emissivity (more strictly emittance) as the ratio of the actual (thermally originated) radiance exiting the cloud to that which would be emitted by a Blackbody at the same temperature. Recalling that the actual thermal radiance exiting the cloud is, by definition, the second term of the (thermal version) of the radiative transfer equation, and the fact that we are dealing with an isothermal cloud, we can immediately write the following expression for the aerosol emissivity over any optical thickness, τ , as

$$\begin{aligned}\epsilon_{\text{aer}}(\tau_o, \omega_o; \tau) &= (1 - \omega_o) \int_0^\tau \frac{J_{\text{int}}(\tau_o, \omega_o; \tau')}{B_{\Delta\lambda}^*(T_{\text{cld}})} e^{-\tau'(\tau_o, r)} d\tau' \\ &= \int_0^\tau \hat{J}_{\text{int}}(\tau_o, \omega_o; \tau') e^{-\tau'(\tau_o, r)} d\tau'\end{aligned}\quad (31)$$

where we have utilized the definition of eq. (28) for the normalized source function in writing the final expression. In eq. (31) it should be clear that J_{int} is the total emissive source function including both direct emissive contribution and the multiple scattering contribution discussed in connection with eq. (11b).

For the reflectivity (more strictly reflectance) we again use the common definition as the ratio of the actual diffuse radiance exiting the cloud to the incident (external sources) radiance. Again for the isotropic case and using the (optical version) of the radiative transfer equation, we can immediately write the following expression for the aerosol reflectivity:

$$\begin{aligned}r_{\text{aer}}(\tau) &= \omega_o \int_0^\tau \frac{J_{\text{ext}}(\tau_o, \omega_o; \tau')}{B_{\Delta\lambda}^*(T_{\text{ext}})} e^{-\tau'(\tau_o, r)} d\tau' \\ &= \int_0^\tau \hat{J}_{\text{ext}}(\tau_o, \omega_o; \tau') e^{-\tau'(\tau_o, r)} d\tau'\end{aligned}\quad (32)$$

where we have again used the definition of eq. (28) for the normalized source function in writing the final expression. It is this definition that led us, early on, to consider only isotropic ambient inputs for the Lambertian sky and surface layers. There is no problem, however, in defining a weighted reflectivity for the non-isotropic case (as we have done elsewhere) but the conclusions are more difficult to deal with.

In figure 6 we show results of calculations of total edge-to-edge cloud emissivity (left) and reflectivity (right) based on the above expressions and utilizing the source functions of figure 5. As before, the various curves in each of the two subplots refer to albedo ranging from $\omega_o = 0$ to 1 in increments of roughly $\Delta\omega_o = 0.10$ with any exceptions so noted. Note the usual reversal in the

ordering of the curves for the two cases wherein the curves decrease in magnitude with increasing albedo for the emissive case, and conversely, increase in magnitude with increasing albedo for the reflective case as seen previously in the behavior of the source functions. Clearly the results are well behaved and qualitatively predictable as we would expect based upon the behavior of the underlying source functions of figure 5.

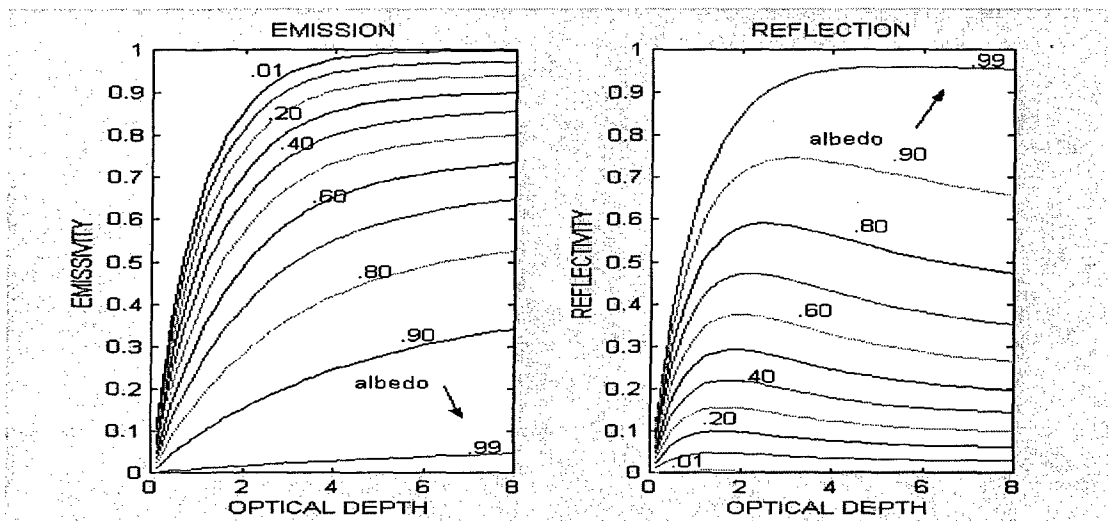


Figure 6. Summary plots of emissivity and reflective for various values of albedo and optical thickness.

Referring first to the emissive results, we see that for all cases the curves show a consistent monotonic increase with increasing optical thicknesses and tend to "level off" as the optical thickness increases, a trend most apparent in the uppermost curves. Note also that as the albedo increases (lowermost curves) the curves become more closely linear and eventually approach a flat line along the zero axis in the extreme ($\omega_0=1$), which we actually demonstrate with the slightly sloped and nearly straight line for $\omega_0=0.99$. Also as one would expect, the emissivity generally approaches unity as the optical thickness increases and the albedo decreases as demonstrated by the uppermost curve.

Referring next to the reflective results, we see that the general behavior is somewhat complimentary to the emissive case but potentially more interesting in that, before leveling off, the curves exhibit a broad peak that appears to be most prominent at the intermediate albedos. In all cases the "peaks" are broad and generally occur at an optical thickness of around a value of $\tau \sim 1-3$, becoming broader and displaced slightly to the higher values as the albedo increases and being essentially "washed out" at the highest albedo. Also in complimentary fashion to the reflective case, the curves become more closely linear as the albedo *decreases* and eventually approach a flat line along the zero axis in the extreme ($\omega_0=0$). The general behavior here is qualitatively similar to the more conventional plane layer results of the literature, but there are substantial quantitative differences that will be discussed more fully in the next section. It also turns out that the "anomalous" broad peak in the reflection functions gives rise to some interesting ramifications in the real world leading, in some cases, to a curious "edge brightening" effect most prominent at the shorter wavelengths [18] and discussed more fully in [5].

Referring back to source functions of figure 5, and noting the apparent trend toward "flatness" at the smaller values of optical thickness, it is immediately clear from the form of eq. (31) and (32)

that in these cases we can move the source function out from under the integral and immediately extract the following very useful approximations:

$$\begin{aligned}\varepsilon_{\text{arc}} &= (1 - \omega_o) \bar{J}_{\text{int}} [1 - \exp(-\tau)] \\ r_{\text{acr}} &= \omega_o \bar{J}_{\text{ext}} [1 - \exp(-\tau)]\end{aligned}\tag{33}$$

where the overbar represents the mean value of the corresponding normalized source function (which will be near unity). Both expressions are *bona fide* first order solutions that also happen to be very accurate for nearly any geometry as long as the optical thickness is small. The expressions also predict a linear form in the extreme as the optical thickness approaches zero which is consistent with the data of figure 6 in the appropriate limit. The approximations fail at the higher optical thickness but do predict asymptotic limits that are at least in qualitative agreement with the exact solutions. It is of some interest to also realize that the above approximations become exact solutions for any case where the source function actually is a constant. One particularly useful situation where this occurs is the case of horizontal path propagation (i.e., $z=\text{constant}$) through a horizontally uniform plane layer. This is a highly useful result that leads to many generalizations based on plane layers that must be used with caution for the case of finite clouds. In the general case the expressions of eq. (33) are most accurately described as the first order, or single-scattering solutions, and are referred to as such throughout the remainder of this paper.

We demonstrate this latter point in the plots of figure 7 where we compare the ratios of the exact solutions with their corresponding single-scattering counterparts for the same range of values used in figure 6. With this ratio as the metric, the plots essentially demonstrate the significance of multiple scattering by the deviations from unity. Note in figure 7 that all curves begin at a value of 1 (perfect agreement) for an optical thickness near zero and go either upward (emissive) or downward (reflective) as the optical thickness increases. It is thus immediately clear that in both cases the errors increase with increasing optical thickness, but the sense of the correction is reversed for the two cases, giving rise to an underestimate (ratio >1) for the emissive case and an overestimate (ratio <1) for the reflective case. The effect of the albedo is also reversed for the two cases in the sense that the emissive errors generally decrease (i.e., approach unity) with decreasing albedo and eventually collapse to unity in the extreme $\omega_o=0$ (pure absorption) whereas the reflective errors generally increase (i.e., again approach unity) with increasing albedo and also eventually collapse to unity in the other extreme $\omega_o=1$ (pure scattering). This circumstance, which may appear confusing at first glance, is more clearly thought of as a manifestation of the fact that the approximate solutions *underestimate* the emissivity but *overestimate* the reflectivity. It is also worth noting that in both cases the curves either rise (emissive) or fall (reflective) from unity beginning at the origin and monotonically increase (emissive) or decrease (reflective), most rapidly at first, but then “level off” at higher optical thicknesses. Also this “leveling off” point is a function of the albedo giving rise to “flatter” curves as the albedo decreases (emissive) or increases (reflective). The general predictive nature and smooth analytical form of the curves suggest the existence of some potential “fixes” that could improve the accuracy of existing models based on first order solutions.

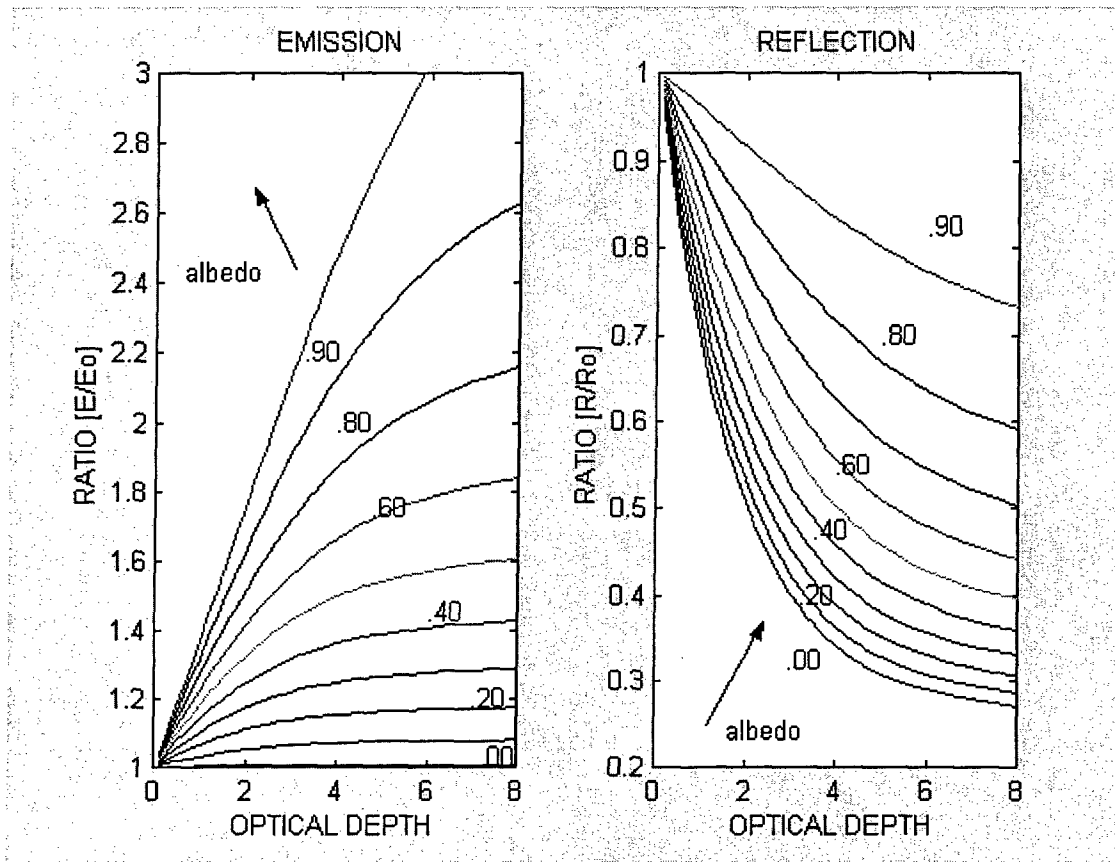


Figure 7. Relationship between exact solutions and one dimensional approximations.

Some of the seemingly contradictory, or at least confusing, behavior of the above results can be made more clear from a closer examination of eq. (29) from which we can derive a very useful relationship between emissivity and reflectivity. To do this we first multiply both sides by the exponential weighting factor, $e^{-\tau(r,r_0)}$, and then integrate as follows:

$$\int_0^{\tau} \hat{J}_{\text{ext}}(\tau_o, \omega_o; \tau') e^{-\tau'(r, r_o)} d\tau' + \int_0^{\tau} \hat{J}_{\text{int}}(\tau_o, \omega_o; \tau') e^{-\tau'(r, r_o)} d\tau' = \int_0^{\tau} e^{-\tau'(r, r_o)} d\tau' \quad (34)$$

from which, with the aid of eq. (31) and (32) and after performing the (trivial) integration on the right side, we arrive at the following very useful expression(s):

$$\begin{aligned} \varepsilon_{\text{aer}}(\tau_o, \omega_o; \tau) + r_{\text{aer}}(\tau_o, \omega_o; \tau) &= (1 - e^{-\tau}) \\ \text{or} \\ \varepsilon_{\text{aer}}(\tau_o, \omega_o; \tau) + r_{\text{aer}}(\tau_o, \omega_o; \tau) + t_{\text{aer}}(\tau) &= 1 \end{aligned} \quad (35)$$

where t_{aer} is defined as the aerosol transmissivity (more strictly transmittance) and is readily calculated from the optical thickness as $[t = \exp(-\tau)]$. Equation (35) is similar in form to the analogous relationship for hard targets [i.e., $\varepsilon_{\text{sfc}} + r_{\text{sfc}} = 1$] and one that turns out to be true not only for spherical aerosol distributions but also for plane layers. It should be noted that even the approximate expressions of eq. (33) obey the relationships of eq. (35); however, this very useful

fact can sometimes cause problems and confusion if care is not taken to understand the origin of the derivation. In the next section we test the various results and relationships by comparing with known solutions from literature.

7. Verification and Comparison with Plane Layers

Although there are some comparable recent developments in modeling finite clouds that we have used for qualitative verification of our results, it turns out that the most extensive quantitative set of data apply to the more common plane layers. In this section we compare results with the extensive and authoritative tables of Van de Hulst [10]. It turns out that, with some minor modification, the methods of Section 3 for spherical symmetry can also be applied to plane layers. In this case we characterize the cloud in terms of the vertical optical depths, τ_v , in place of the centerline value used for spherical symmetry. In this case the angular dependence is derived from the relationship, $[\tau(\mu)=\tau_v/\mu]$ where μ is the slant path cosine referenced with respect to the outward normal, thus the azimuth integration method of Section 3 remains valid. Further details on the other modifications needed are given in [5].

Results of our comparison with plane layers are shown in Table 1, where, out of curiosity, we also show results for comparable spheres and results using the approximations of eq. 33. The layout of Table 1 follows the general scheme of Van de Hulst and provides for five subtables covering a range of albedos from $\omega_0=1$ (extreme top) to $\omega_0=0$ (extreme bottom) and, in each case, six values of total cloud optical thickness ranging from 0.125 (top) to 4.0 (bottom). As usual, we include both the reflective (left) and emissive (right) cases. For the spherically symmetric case the total optical depth refers to the edge-to-edge values passing along the cloud centerline as we have done throughout.

Table 1. Comparisons with plane layers.

$\omega_0=1.0$								
REFLECTIVITY					EMISSIONITY			
Tau	Plane1	Plane2	Sphere	Eq. 33a	Plane1	Plane2	Sphere	Eq. 33b
.12500	.11750	.11750	.11751	.11750	.00000	.00000	.00001	.00000
.25000	.22120	.22120	.22122	.22120	.00000	.00000	.00002	.00000
.50000	.39347	.39347	.39360	.39347	.00000	.00000	.00013	.00000
1.00000	.63212	.63212	.63234	.63212	.00000	.00000	.00022	.00000
2.00000	.86466	.86466	.86497	.86466	.00000	.00000	.00031	.00000
4.00000	.98167	.98167	.98199	.98168	.00001	.00000	.00033	.00000
$\omega_0=0.80$								
Tau	Plane1	Plane2	Sphere	Eq. 33a	Plane1	Plane2	Sphere	Eq. 33b
.12500	.08978	.08978	.09311	.09400	.02772	.02772	.02439	.02350
.25000	.16305	.16305	.17359	.17696	.05815	.05815	.04761	.04424
.50000	.27139	.27139	.30274	.31478	.12208	.12208	.09073	.07869
1.00000	.38439	.38437	.46561	.50570	.24773	.24775	.16651	.12642
2.00000	.41663	.41655	.58235	.69173	.44803	.44811	.28231	.17293
4.00000	.34105	.34079	.56188	.78535	.64063	.64089	.41980	.19634
$\omega_0=0.40$								
Tau	Plane1	Plane2	Sphere	Eq. 33a	Plane1	Plane2	Sphere	Eq. 33b
.12500	.04119	.04119	.04568	.04700	.07631	.07631	.07182	.07050
.25000	.07046	.07046	.08358	.08848	.15074	.15074	.13762	.13272
.50000	.10648	.10647	.14001	.15739	.28699	.28700	.25346	.23608
1.00000	.13056	.13055	.19982	.25285	.50156	.50157	.43230	.37927
2.00000	.11971	.11966	.21910	.34587	.74495	.74500	.64556	.51880
4.00000	.09234	.09221	.18004	.39267	.88934	.88947	.80164	.58901
$\omega_0=0.20$								
Tau	Plane1	Plane2	Sphere	Eq. 33a	Plane1	Plane2	Sphere	Eq. 33b
.12500	.01987	.01978	.02263	.02350	.09772	.09772	.09487	.09400
.25000	.03295	.03295	.04095	.04424	.18821	.18825	.18025	.17696
.50000	.04808	.04808	.06749	.07869	.34539	.34539	.32598	.31478
1.00000	.05637	.05636	.09323	.12642	.57575	.57576	.53889	.50570
2.00000	.04980	.04977	.09728	.17293	.81486	.81489	.76738	.69173
4.00000	.03847	.03841	.07666	.19634	.94321	.94327	.90502	.78535
$\omega_0=0.0$								
Tau	Plane1	Plane2	Sphere	Eq. 33a	Plane1	Plane2	Sphere	Eq. 33b
.12500	.00000	.00000	.00000	.00000	.11750	.11750	.11750	.11750
.25000	.00000	.00000	.00000	.00000	.22120	.22120	.22120	.22120
.50000	.00000	.00000	.00000	.00000	.39347	.39347	.39347	.39347
1.00000	.00000	.00000	.00000	.00000	.63212	.63212	.63212	.63212
2.00000	.00000	.00000	.00000	.00000	.86466	.86466	.86466	.86466
4.00000	.00000	.00000	.00000	.00000	.98168	.98168	.98168	.98168

It is immediately clear from inspection of the plane layer results that our values (labeled Plane1) are virtually identical to those of Van de Hulst (labeled Plane2), most often showing agreement to within 4–5 significant figures. The major discrepancies occur at higher optical thickness and higher albedos, which is expected because of the increase of multiple scattering.

Referring first to the uppermost subtable, representing the extreme conservative case ($\omega_0=1$), it is immediately apparent that *all* methods, including the simple first order approximations, give nearly identical answers, a fact that seems strange at first since we are dealing with the extreme multiple scattering case where “approximations” should not necessarily work that well. The reason this happens, however, was made clear from the preceding discussion of the source functions of figure 5 that, as we pointed out, *all* collapse to unity in the extreme conservative

case, independent of the optical thickness. In this case (i.e., all $J=\text{Constant}$) the line integrations are trivial and reduce to the form of eq. (33), independent of cloud geometry. In Table 1 there is, in fact, some slight difference in the spherical case results that we later found to be due to numerical integration procedures that we have subsequently corrected. For the emissive case it is, of course, clear that all results agree because of the prefactor, $1-\omega_o=0$, leading to the trivial solutions that are identically zero.

Referring next to the bottommost subtable, representing the opposite extreme for pure absorption ($\omega_o=0$), we also find (nearly) identical answers in all cases, including the trivial zero solutions for the reflective case. We also note that the emissive solutions for the pure absorption (lower right table) are identically equal to the corresponding reflective solutions for pure scattering (upper left table) which is the expected result that follows from the respective extreme case trivial solutions represented by eq. (33).

For the intermediate cases in Table 1 it is significant that the spherical results agree extremely well with the plane layer results at the lower optical thicknesses. This is, of course, a manifestation of the fact that for both cases the source functions are essentially flat, and thus even the first order "approximations" work well. At the higher optical thickness the differences do become significant and generally show a higher reflectivity and lower emissivity for the spherical results as compared to the plane layer results. This behavior can be understood from geometrical considerations and is intuitively clear. It is also significant and consistent with earlier discussions that eq. 33 works well for small optical thickness, but overestimates reflectivity and underestimates emissivity at the higher optical thickness and performs best at the lowest albedo. Upon a close inspection of the numerical results of table 1, we also note that emissivity functions, except for the trivial cases, all show a monotonic increasing behavior with respect to optical thickness. However, except for the extreme conservative case, we again note the curious "peak" in the reflectance data at an optical thickness around a value of $\tau=2$ that was noted earlier in figure 6.

It seems clear that the results of Table 1 (both quantitative and qualitative) leave little doubt as to the validity of the method. Further quantitative comparisons with the plane layer results and some quantitative comparisons with spherical and cylindrical results are given in [5].

8. Applications: Effects On IR Scene Modeling

The ultimate application of the methods described here lies in the utility for IR scene generation in support of electromagnetic systems analysis. These modeling, or simulation, exercises usually begin with some arbitrary baseline "clear air" scene, either measured or synthetically generated, in the form of a digital array which we call the "background" array (which includes the "target" somewhere within). We then integrate effects of obscurants, element by element, using the methods outlined and most explicitly expressed by eq. (30). Some examples using a 100 by 100 m pixel array and a Gaussian aerosol cloud 50 m in radius is shown in figure 8.

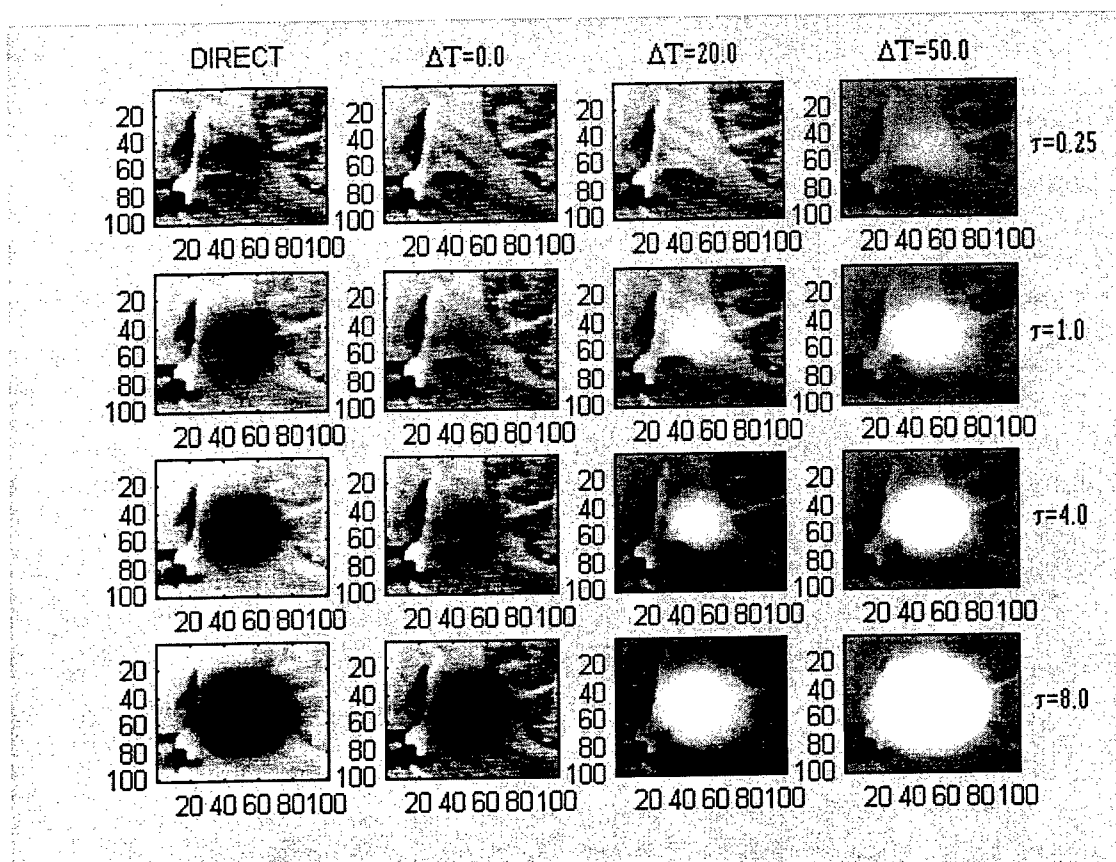


Figure 8. Effect of cloud temperature on IR scene imagery.

The examples of figure 8 cover four optical thicknesses (rows) and three cloud temperature differentials (columns) as indicated in the headings and margins. The first column is an exception which corresponds to the direct (Beer's Law) component only which we could take as corresponding (strictly) to cloud and ambient temperatures of absolute zero. The particular background scene used here has no particular significance to the problem except to serve as an illustrative aid; however, we did normalize the array such that the average pixel radiance corresponds to a temperature equal to that of the ambient temperature, which we chose to be 20 °C. Temperature differences labeled above each column correspond to differentials above the ambient [$\Delta T = T_{\text{cld}} - T_{\text{amb}}$]. The four optical thicknesses represent the total edge-to-edge values passing through the cloud centerline as we have done throughout. In all cases we used a cloud albedo of $\omega_0 = 0.50$, which represents a compromise between the extremes.

For the direct component (first column), the effect of an increased optical thickness is, of course, an increased reduction in radiance, or darkening, and the subsequent impression of a larger effective cloud as the optical depth increases. The second column represents the "equilibrium" case wherein the cloud temperature is equal to the ambient temperature [i.e., $\Delta T = 0$], which, in this example, happens to also be equal to the average of the scene temperature (i.e., all temperatures are 20 °C). We see in this case (second column) that the effect of adding the diffuse component, even when there is no temperature differential, is to (partially) compensate the effect of the direct component so that the resultant appearance is a less-darkened cloud image. This "compensation," however, only adds noise from the cloud and does not in any way restore the direct signal. From examination of the remaining columns we see the effect of an increased

“whitening” as the cloud temperature is increased to the point where we are left with a “hot” image dominated by the cloud emission that appears to totally obscure the scene at the extreme.

Perhaps the most curious aspect of the results in figure 8 is the apparent compensating action of the path radiance which tends to “cancel” the effect of direct extinction. According to the model, there can be found a particular cloud temperature wherein the path radiance would completely offset the loss due to direct extinction, giving a result identical *in appearance* to the original unobscured case. This is nearly the case for the lower extremes in the example. In reality, however, there is actually a big difference between the two cases because most of the received signal in the obscured case comes from the cloud and is thus “noise” to the sensor as described earlier. The usable “signal” comes only from the direct component and is independent of cloud temperature. The “lesson” to be learned from this example is to recognize that it is the aerosol “noise,” that can often determine systems performance, especially for the case of hot emissive smokes found in the U.S. Army inventory and elsewhere. Some further insights into how one might quantify the effect are suggest in [5] and to some lesser extent in the next section.

9. Summary and Discussion

Our method for generating exact analytical solutions for both the optical and thermal versions of the radiative transfer equation offers a viable and robust methodology for calculating emissivities and reflectivities of radially symmetric, finite-sized clouds of arbitrary optical thickness and albedo. Direct comparisons with known solutions show the method to be accurate to within 4–5 significant figures and all results are consistent with fundamental principles and known asymptotic behavior. The results also help verify and define the quantitative limits of the approximations often used throughout the literature and offer a baseline for incorporating effects of multiple scattering and thermal emission that are often not treated in many contemporary obscuration studies.

A major advantage offered by the method that may have been missed in the main text is the benefit from using the source function approach and the characterization in terms of the optical thickness (rather than spatial distance). It turns out that the curves of figure 5 are much more universal than one may think. For example; if we worked the problem for a cloud, say, the size of a basketball and then let the cloud grow uniformly to the size of, say, a football arena the source function, if characterized in terms of the optical thickness *would be the same*. This inherent robustness in the approach seems to be either missed or ignored in many contemporary models.

A major disadvantage of the approach, *per se*, is that although the methods offer exact solutions, they are rigorously correct only for certain idealized geometries of plane, spherical, or cylindrical clouds. We have also restricted the results here to Gaussian concentration distributions; however this turns out to be a relatively unimportant detail as nearly any distribution could be used as long as symmetry is maintained. These particular disadvantages can be addressed using any number of novel approximations worked out by modelers over the years. One of our own future objectives is to apply geometric perturbations, such as fractal and spectral methods [19] to add

statistical realism to our idealized Gaussian clouds. In other papers we have also investigated approximate methods for incorporating non-isotropic scattering effects and non-isotropic boundary conditions to accommodate direct beam (solar) in-scatter, which our studies show can be important at the shorter wavelengths [3].

The usefulness of the data contained herein in supporting IR scene generation initiatives is amply demonstrated in Section 8 figures and this is the main goal of the effort. However, there are other applications where the information may be helpful in estimating the general effects on real IR systems. In the more comprehensive models, a key parameter is the signal-to-noise ratio [20], or scene contrast, which can be written in the context of our terminology as

$$C(\tau) = \left\{ \frac{e^{-\tau} B_{\Delta\lambda}^*(T_{tgt})}{\epsilon_{aer}(\tau) B_{\Delta\lambda}^*(T_{cld}) + r_{aer}(\tau) B_{\Delta\lambda}^*(T_{ext}^*) + R_{sys}} \right\} \{C(\tau = 0)\} \quad (36)$$

where $C(\tau=0)$ is the differential IR scene contrast as measured at the (unobscured) target/back-ground surface and R_{sys} is the system noise used in conventional "clear air" studies. All other quantities are defined in previous sections. It is significant that the noise term in the denominator includes both a system induce component and an aerosol-induced component. In the past the analyst has often been forced to overlook this aerosol-induced component, or resort to questionable assumptions concerning the effects of emissivity and multiple scattering. We believe that the results here can help remove this barrier in a wide variety of technical applications.

References

1. Jacobs, P.A., *Thermal Infrared Characterization of Ground Targets and Backgrounds*, SPIE Optical Engineering Press, Bellingham, WA (USA), 1996.
2. Hoock, D.W. and R.A. Sutherland, "A Combined obscuration Model for Battlefield Induced Contaminants, COMBIC," ASL-TR-0213, 1984.
3. Sutherland, R.A., Thompson, J.C. and S.D. Ayres, "Infrared Scene Modeling in Emissive, Absorptive, and Multiple Scattering Atmospheres," Proceedings of SPIE, April 2001.
4. Sutherland, R.A., Thompson, J.C. and J.D. Klett, "Effects of Multiple Scattering and Thermal Emission on Target-Background Signatures Sensed through Obscuring Atmospheres," Proceedings of SPIE, April 2000.
5. Sutherland, R.A., "Verification of the Aerosol Emissivity Model, PILOT-EX," ARL-TR-2689, June 2001.
6. Sutherland, R.A., "Broadband and Spectral Emissivities of some Natural Soils and Vegetation," J. Atmos. Tech., 3(1), 199-202, 1986.
7. Wolfe, W. L., *Radiation Theory*, Ch. 1, Vol. 1, The Infrared and Electro-Optical Systems Handbook, SPIE Press, Bellingham, WA (USA), 1993.
8. Hoock, D.W. and R.A. Sutherland, *Obscurant Countermeasures*, Ch. 6, Vol. 7, The Infrared and Electro-Optical Systems Handbook, SPIE Press, Bellingham, WA (USA), 1993.
9. Bohren, C.F. and D.R. Huffman, *Absorption and Scattering of Light by Small Particles*, John Wiley & Sons, 1983.
10. Van de Hulst, H.C., *Multiple Light Scattering Tables, Formulas, and Applications, Vol 1*, Academic Press, 1983.
11. Chandrasekhar, S., *Radiative Transfer*, Dover Publications, New York, 1960.
12. Turner, R.E., "Radiation in Finite Clouds: Diffusion Model," Contract Report, U.S. Army Research Office, Contract No. DAAL03-86-D-0001, DO No. 0689, January 1989.
13. Thynell, S.T. and M.N. Ozisik, "Radiation Transfer in Absorbing, Emitting, Isotropically Scattering, Homogeneous Cylindrical Media," J. Quant. Spectrosc. Transfer, 38(6):413-426, 1987.
14. Evans, K.F., "The Spherical Harmonic Discrete Ordinate Method for Three-dimensional Atmospheric Radiative Transfer," Journal of the Atmospheric Sciences, 55,429-446,1998.
15. Kondratyev, K. Ya, *Radiation in the Atmosphere*, Academic Press, New York and London, 1969.
16. Farmer, W. M., "Analysis of emissivity effects on target detection through smoke/obscurants," Opt. Eng., 30(11), 1701-1708, 1991.
17. Davis, R.E., "Modeling Emissive Sources," Special report for ARL/BE, November 1995.

18. Sutherland, R.A., 1982, "Field measurement requirements for electro-optical obscuration modeling," Proceedings of the Society of Photo-Optical Instrumentation Engineers, 356:14-20.
19. O'Brien, S.G. and D.W. Hoock, 1998, "STATBIC-A Method for Inclusion of Fractal Statistics in Obscurant Transport Models," ARL-TR-1375, April 1998.
20. Holst, G.C., "Common Sense Approach to Thermal Imaging," SPIE Press, Bellingham WA, 98227-0010, 2000.

REPORT DOCUMENTATION PAGE				<i>Form Approved</i> OMB No. 0704-0188	
Public reporting burden for this collection of information is estimated to average 1 hour per response, including the time for reviewing instructions, searching existing data sources, gathering and maintaining the data needed, and completing and reviewing the collection information. Send comments regarding this burden estimate or any other aspect of this collection of information, including suggestions for reducing the burden, to Department of Defense, Washington Headquarters Services, Directorate for Information Operations and Reports (0704-0188), 1215 Jefferson Davis Highway, Suite 1204, Arlington, VA 22202-4302. Respondents should be aware that notwithstanding any other provision of law, no person shall be subject to any penalty for failing to comply with a collection of information if it does not display a currently valid OMB control number. PLEASE DO NOT RETURN YOUR FORM TO THE ABOVE ADDRESS.					
1. REPORT DATE (DD-MM-YYYY) July 2002		2. REPORT TYPE Final		3. DATES COVERED (From - To) August 1998–October 2001	
4. TITLE AND SUBTITLE Determination and use of IR Band Emissivities in a Multiple Scattering and Thermally Emitting Aerosol Medium				5a. CONTRACT NUMBER	
				5b. GRANT NUMBER	
				5c. PROGRAM ELEMENT NUMBER	
6. AUTHOR(S) Sutherland, Robert A.				5d. PROJECT NUMBER	
				5e. TASK NUMBER	
				5f. WORK UNIT NUMBER	
7. PERFORMING ORGANIZATION NAME(S) AND ADDRESS(ES) U.S. Army Research Laboratory Information & Electronic Protection Division Survivability Lethality Analysis Directorate (ATTN: AMSRL-SL-EM) White Sands Missile Range, NM 88002-5513				8. PERFORMING ORGANIZATION REPORT NUMBER ARL-TR-2688	
9. SPONSORING/MONITORING AGENCY NAME(S) AND ADDRESS(ES) U.S. Army Research Laboratory 2800 Powder Mill Road Adelphi, MD 20783-1145				10. SPONSOR/MONITOR'S ACRONYM(S)	
				11. SPONSOR/MONITOR'S REPORT NUMBER(S) ARL-TR-2688	
12. DISTRIBUTION/AVAILABILITY STATEMENT Approved for public release; distribution unlimited.					
13. SUPPLEMENTARY NOTES					
14. ABSTRACT <p>We report on the application of a fast and efficient method for producing exact solutions of the thermal version of the radiative transfer equation, including effects of multiple scattering from both interior (thermal) sources and exterior (ambient) sources. The method is accurate to within four significant figures when compared with plane layer solutions published in the literature; this method has the added capability for treating discrete, localized aerosol clouds of spherical (and cylindrical) symmetry. The method, briefly summarized and applied in earlier papers, is described in detail here where we also demonstrate the utility of the method for calculating emissivity (and reflectivity) functions for finite aerosol clouds of arbitrary optical thickness and albedo. This report is focused on concepts and methods of the PILOT-EX model, which forms the theoretical basis for the more practical aerosol effects model PILOT81 designed for use in infrared scene generation and systems analysis.</p>					
15. SUBJECT TERMS emissivity, multiple scattering, thermal emission, atmospheric obscurants, aerosols, smoke, clouds, modeling, simulation					
16. SECURITY CLASSIFICATION OF:			17. LIMITATION OF ABSTRACT SAR	18. NUMBER OF PAGES 41	19a. NAME OF RESPONSIBLE PERSON R.A. Sutherland
a. REPORT U	b. ABSTRACT U	c. THIS PAGE U			19b. TELEPHONE NUMBER (Include area code) (505) 678-4520